

This paper must be cited as:

V. Vera, D. Mendez-Gonzalez, D. J. Ramos-Ramos, A. Igalla, M. Laurenti, R. Contreras-Caceres, E. Lopez-Cabarcos, E. Díaz, J. Rubio-Retama, S. Melle, O. G. Calderón; *Journal of Materials Chemistry C* 2021, doi: 10.1039/D1TC01419F

V. Vera, D. Mendez-Gonzalez, D. J. Ramos-Ramos, A. Igalla, M. Laurenti, R. Contreras-Caceres, E. Lopez-Cabarcos, E. Díaz, J. Rubio-Retama, S. Melle, O. G. Calderón

E-mail: oscargc@ucm.es

This document is the unedited Author's version of a Submitted Work that was subsequently accepted for publication in *Journal of Materials Chemistry C*, copyright © Royal Society of Chemistry after peer review. To access the final edited and published work see:

<https://pubs.rsc.org/en/content/articlelanding/2021/tc/d1tc01419f>

Cite this: DOI: 00.0000/xxxxxxxxxx

Effect of dopant concentration and excitation intensity on the up-conversion and downconversion emission of β -NaYF₄:Yb³⁺,Er³⁺ nanoparticles[†]Vivian Torres Vera,^a Diego Mendez-Gonzalez,^a Diego J. Ramos,^{b,c} Asmae Igalla,^b Marco Laurenti,^{a,d,e} Rafael Contreras-Caceres,^a Enrique Lopez-Cabarcos,^a Elena Díaz,^c Jorge Rubio-Retama,^{a,e} Sonia Melle,^b and Oscar G. Calderón,^{*b}Received Date
Accepted Date

DOI: 00.0000/xxxxxxxxxx

The dopant concentration of lanthanide ions in photon-upconversion nanoparticles (UCNPs) remains one of the key points to boost these nanomaterials' brightness and, therefore, their application development. Here, we analyzed the effect of Er³⁺ and Yb³⁺ dopant concentration of β -NaYF₄:Yb³⁺,Er³⁺ nanoparticles on the visible upconversion and near-infrared downconversion luminescence intensity. To maintain the size and the morphological properties of the nanoparticles we used a total dopant concentration of 22% while varying the ratio of Yb³⁺ to Er³⁺ ions from 0 to 10. A huge increase in luminescence takes place as the Yb/Er ratio increases following a power-law behavior, being this luminescence enhancement greater at low excitation intensities. Above an Yb/Er ratio around two, saturation occurs with a slight peak when this ratio is around four. Simulations using a rate equation model showed that upconversion luminescence (UCL) is mainly produced by energy transfer between neighboring Er³⁺ ions at low Yb/Er ratios, while at high ratios, energy transfer from Yb³⁺ to Er³⁺ ions dominates. However, downconversion luminescence (DCL) is produced at all analyzed ratios, except 0, by this last mechanism.

1 Introduction

Nanocrystals doped with trivalent rare-earth ions are fascinating photoluminescence probes due to their alluring ability to produce photon upconversion without the need for expensive high-intensity excitation lasers such as those required for two-photon absorption or second harmonic generation.^{1–3} Besides that, rare-earth nanoparticles show large Stokes shifts, lack of photobleaching, absence of blinking, long fluorescent lifetimes, sharp emission bandwidths, and emission tuning capacity, which make them very attractive materials for a pleiad of applica-

tions such as optical imaging probes⁴, biolabeling⁵, sensing⁶, anti-counterfeiting⁷, solar cells⁸, small drug delivery systems⁹, or nanothermometry¹⁰, proving their tremendous scientific and technological potential.

Among the different photon upconversion mechanisms in lanthanide ions as excited-state absorption (ESA), cooperative sensitization upconversion (CSU), cross-relaxation upconversion (CRU), or energy transfer upconversion (ETU), the latter is, by far, the most efficient one.^{11,12} ETU requires two types of ions named sensitizers and activators, inserted into a low-phonon energy matrix. Sensitizer ions, typically Nd³⁺ or Yb³⁺ ions, absorb the excitation photons and transfer the energy to activator ions. The most common activators are Er³⁺, Tm³⁺, or Ho³⁺, and they are characterized by exhibiting ladder-like arranged energy levels, which are essential to facilitate the successive energy-transfer steps that populate higher energy levels and that, upon relaxation, release upconverted photons.¹³ One of the most studied systems is based on NaYF₄:Yb³⁺,Er³⁺ nanoparticles, due to its high upconversion efficiency which, among other factors, is related to the low phonon energy of the host matrix (around 360 cm⁻¹).¹⁴ After excitation with a continuous wave (CW) laser at 980 nm, these nanoparticles exhibit three prominent upconversion bands located at the blue (410 nm), green (520 and 540 nm), and red (650 nm) wavelengths. Their intensities are very

^a Department of Chemistry in Pharmaceutical Sciences, Complutense University of Madrid, E-28040 Madrid, Spain

^b Department of Optics, Complutense University of Madrid, E-28037 Madrid, Spain. E-mail: oscargc@ucm.es

^c GISC, Department of Materials Physics, Complutense University of Madrid, E-28040 Madrid, Spain

^d Instituto de Ciencia de Materiales de Madrid, c/Sor Juana Inés de la Cruz, Cantoblanco, E-28049, Madrid, Spain

^e Nanobiology Group, Instituto Ramón y Cajal de Investigación Sanitaria, IRYCIS, E-28034, Madrid, Spain

[†] Electronic Supplementary Information (ESI) available: EDS measurements: estimation of Yb³⁺/Er³⁺ dopant ratios; XRD measurements: crystalline phase for UCNPs with different Yb³⁺/Er³⁺ ratios; TEM images showing nanoparticle size histograms for UCNPs with different Yb³⁺/Er³⁺ ratios; Parameter values used in the theoretical model. See DOI: 00.0000/00000000.

sensitive to variations in the surface area-to-volume ratio,¹⁵ crystal structure,¹⁶ lanthanide doping concentration¹⁷ as well as to the ligand and surrounding medium.^{18–20} All these factors define the luminescence efficiency of upconversion nanoparticles (UCNPs). For this reason, understanding the role of these factors in the whole process would be desirable for a rational design of high luminescent UCNPs.

One of the most important factors affecting luminescence efficiency is the lanthanide doping concentrations. Optimal dopant concentrations of 2% Er³⁺ and 18% Yb³⁺ have been reported by Güdel *et al* in order to get the most-efficient near infrared (NIR) to green upconversion in NaYF₄ microcrystals.^{14,21,22} In the case of single-core nanoparticles, several works have evaluated the influence of the Er³⁺ and Yb³⁺ concentration on luminescence properties. In general, an optimal Yb³⁺ concentration between 17%-20% is assumed while the Er³⁺ concentration is kept relatively low (around 2%-4%) to guarantee the distance between dopants and thus to minimize the energy loss resulting from cross-relaxation.^{23–26} For example, Wang *et al.*²³ found that green-fluorescence lifetime of NaYF₄:Yb/Er nanoparticles increases when diminishing Er³⁺ concentration from 32% down to 0.5% while keeping constant Yb³⁺ concentration at 20%. Cao *et al.*²⁵ studied powders samples of NaYF₄ doped with 2% of Er³⁺ and a wide range of Yb³⁺ codoping concentrations finding that the strongest visible emission occurs at 20% of Yb³⁺, since a greater increase in Yb³⁺ concentration induces a transition from hexagonal to cubic phase, thus decreasing the fluorescence emission. Other work by Kaiser *et al.*²⁶ found a maximum particle brightness for UCNPs doped with 14% of Yb³⁺ and 3% of Er³⁺ at low excitation intensities. Recently, the influence of doping concentration on the green/red emission ratio was studied finding that an increase of Yb³⁺ contents from 2 to 25 mol % induced a tunable emission from green to red, being the highest red/green ratio achieved for 1% Er³⁺ and 20% Yb³⁺.²⁷ On the other hand, core/shell structured UCNPs have also shown the ability to enhance their upconversion luminescence by increasing the Yb³⁺ doping level to very high values.^{28,29}

UCNPs not only show upconversion luminescence (UCL), but they have even more efficient downconversion luminescence (DCL) in the near infrared (NIR) which make them ideal candidates for NIR to NIR-DC bioimaging applications.^{30,31} Interestingly it has also been reported that UCL and DCL emission depend on the size of the NaYF₄:Yb³⁺,Er³⁺ nanoparticles. UCL intensity increase as the nanoparticles' size increases, whereas in DCL, the most efficient emission occurs for diameters ranging from 15nm to 40 nm when high excitation intensities are used.³² Similarly, DCL and UCL might show different Yb³⁺/Er³⁺ doping-ratio dependence since different energy levels are involved in the upconversion and downconversion emission processes. Therefore, understanding the NIR-DCL dependence with doping ratio is still needed for optimizing UCNPs use in bioimaging applications. Only a few works deal with the effect in the upconversion and downconversion emission using broader variations in the dopants concentrations and even less analyzing the emission properties above and below the saturation excitation intensity.

Our aim in this work is to test the robustness of the optimal

concentrations of Er³⁺ and Yb³⁺ ions that lead to the highest UCL and DCL. To isolate the effect of ion concentration we synthesized monodisperse NaYF₄:Yb³⁺,Er³⁺ nanoparticles with identical size (30nm), same morphological properties (β -phase), and equal total amount of dopants in the matrix. We fixed the sum of Yb³⁺ and Er³⁺ dopant ions concentration to 22%, in relation to the total ion concentration (Y³⁺ + Yb³⁺ + Er³⁺ = 100%) while testing different Yb³⁺/Er³⁺ ratios ranging from the extreme case where only Er³⁺ ions are present, to ratio 10. We evaluated the composition and the excitation intensity influence on the upconversion and downconversion processes within these broad ratios range while keeping the total amount of dopants in the matrix constant. A rate equation analysis was performed to reproduce the experimental findings. This theoretical analysis allowed us to study the role of the different mechanisms involved in both UCL and DCL processes as the ion dopant concentration was changed.

2 Experimental section

2.1 Chemicals

Ytterbium (III) chloride hexahydrate (99.9%) (YbCl₃·6H₂O), Yttrium (III) chloride hexahydrate (99.9%) (YCl₃·6H₂O), Erbium (III) chloride hexahydrate (99.9%) (ErCl₃·6H₂O), Sodium hydroxide (NaOH) (\geq 98%), Ammonium fluoride (NH₄F) (\geq 98%), Oleic acid (OA) (\geq 90% GC), 1-Octadecene (ODE) (technical grade 90%), Methanol (MeOH) (\geq 99.9% HPLC), Ethanol absolute (EtOH), n-Hexane (\geq 97% GC). All the reagents were purchased from Sigma-Aldrich and used as we received them.

2.2 Synthesis of NaYF₄: Yb³⁺, Er³⁺ UCNPs

Monodisperse β -NaYF₄:Yb_x,Er_y with different dopant ratios were synthesized following the thermal co-precipitation method.³³ First, yttrium(III) chloride hexahydrate (236.63 mg, 0.78 mmol), ytterbium (III) chloride hexahydrate, and erbium (III) chloride hexahydrate were dissolved in 1 mL of MeOH. Afterwards, the rare earth methanol solution was mixed with 1-octadecene (15 mL, 46.9 mmol) and oleic acid (6 mL, 19 mmol) in a three-neck round bottom flask, under moderate stirring. The resulting mixture was heated to 140°C under nitrogen flow at a heating rate of 5°C/min with a heating mantle (Nahita Blue, Serie 656) coupled to a temperature controller (JP selecta). At this point, traces of HCl and solvents were removed by using a vacuum pump during 20 min. The next step was to add 10 mL of methanol solution containing NaOH (100 mg, 2.5 mmol) and NH₄F (148.16 mg, 4.0 mmol), letting the reaction to incubate for 30 minutes. The temperature was increased again to 110°C with a heating rate of 4°C/min under N₂ flow. Again vacuum pump was used during 20 min. Finally, the solution was heated until it reached a temperature of 316°C and refluxed for 1h.

After the solution was cooled down to room temperature, nanoparticles were purified by splitting the product into four centrifuge tubes and vigorously mixing them with 4 mL of MeOH. Subsequently, the phases were allowed to separate, and the methanol phase was removed. Then, the sample was centrifuged at 8500 rpm for 20 minutes. The pellet was washed with 1 mL EtOH twice, without redispersing it. The pellet was finally dried

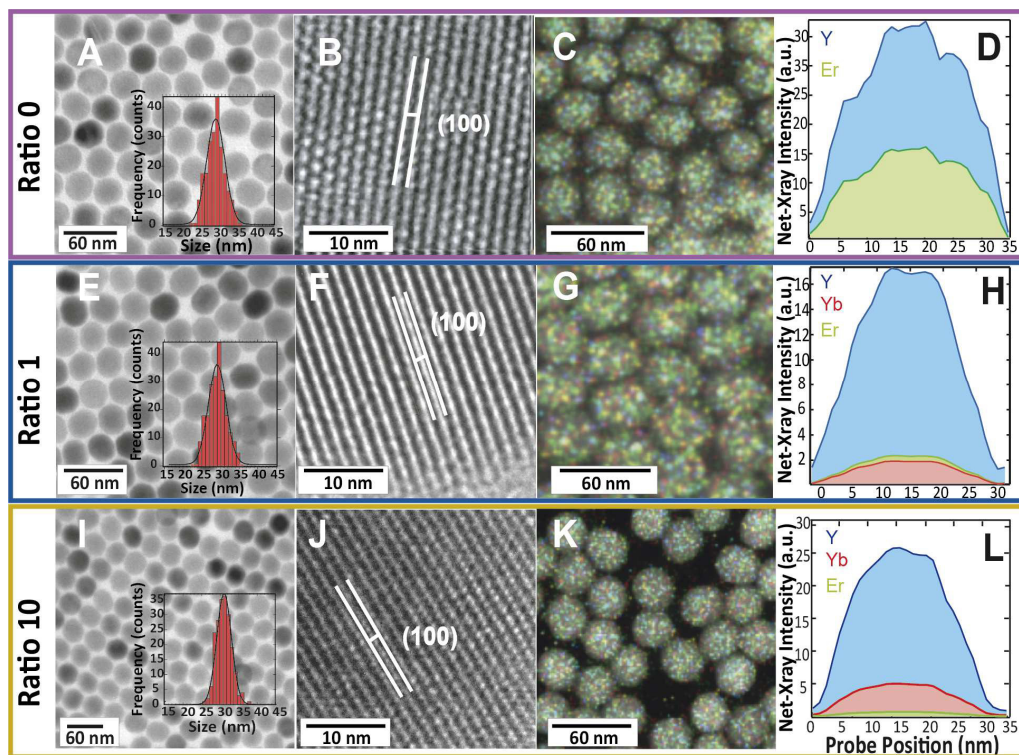


Fig. 1 TEM micrographs of the synthesized nanoparticles (A, E, and I), the inset in each figure shows the size distribution of the nanoparticles. A detailed crystalline nanoparticle structure shows the lattice fringe (100) obtained by HR-TEM (B, F, and J). Elemental mapping micrograph of the obtained nanoparticles (C, G, and K). Element distribution profile of the doping ions within each nanoparticle (D, H, and L). Figures A, B, C, and D correspond to the nanoparticles doped with Er^{3+} exclusively (Yb/Er ratio 0). Figures E, F, G and H correspond to nanoparticles doped with Yb^{3+} and Er^{3+} at a Yb/Er ratio of 1, and Figures I, J, K, and L correspond to nanoparticles doped with Yb^{3+} and Er^{3+} at a Yb/Er ratio of 10.

and dispersed in 4 mL of hexane for storage. Table 1 shows the different $\text{Yb}^{3+}/\text{Er}^{3+}$ dopant ratios synthesized in this work.

Table 1 Relation between the number of moles of dopants used. In all cases, the number of moles of Y^{3+} remained constant at 0.78 mmol where 100% corresponds to the sum of the moles of Y^{3+} , Yb^{3+} , and Er^{3+} ions.

Ratio $\text{Yb}^{3+}/\text{Er}^{3+}$	Yb^{3+} (mmol)	Yb^{3+} (%)	Er^{3+} (mmol)	Er^{3+} (%)
10	0.200	20.0	0.020	2.0
8	0.196	19.6	0.024	2.4
4	0.176	17.6	0.044	4.4
1	0.110	11.0	0.110	11.0
0.25	0.044	4.4	0.176	17.6
0.12	0.024	2.4	0.196	19.6
0.1	0.020	2.0	0.200	20.0
0	0	0	0.220	22.0

2.3 Characterization

2.3.1 Morphological Characterization

Chemical and morphological characterization of the UCNP was carried out using a JEOL JEM 1010 electron transmission microscope (TEM) working at a voltage of 80 kV. High-resolution images were taken (HR-TEM) with a microscope JEOL JEM 2100 under a working voltage of 200 kV. High-angle annular dark-field (HAADF) scanning TEM and EDX mappings have been realized using an FEI Talos F200X (FEI, USA, 80 kV) coupled to an EDX

detector. All samples were prepared by adding 10 μL of the UCNP solution (ca. 3 mg/mL) on a Cu grid and letting the solvent to evaporate at room temperature. To determine the crystalline phase, X-ray diffraction (XRD) patterns of dried UCNP powders were recorded with a PANalytical Model X'Pert PRO MPD Multi-Purpose Diffractometer.

2.3.2 Optical Characterization

The luminescence emission spectra of UCNP were measured with a fluorescence home-built system described previously³⁴ (see scheme in Figure 2A). Briefly, the beam from a 976 nm pigtailed 10 W CW excitation laser (JDSU, L4-9897603) provided with a current and temperature controller (ILX Lightwave, LDX-36025-12, and LDT-5525B, respectively) is transmitted through a long-pass dichroic filter (Semrock, FF757-Di01), and then focused on a micro-cuvette (Hellma 101.015-QS, 3 mm optical path) with a 10x objective. The luminescence coming from the sample is reflected by the dichroic mirror towards a short-pass filter, which blocks the reflected radiation between 770 nm and 1050 nm (Semrock, FF01-775/SP). The beam is then focused into an optical fiber connected to a monochromator (Horiba Jobin Yvon, iHR320). The monochromator uses an 1800 gr per mm grating blazed at 500 nm and a photomultiplier tube (Hamamatsu, R928) to measure upconversion luminescence in the green (520-570nm) and red (640-660nm) emission bands of the UCNP. IR down conversion spectra (1525-1575 nm) is measured using an

InGaAs solid-state detector (Horiba Jobin Yvon, DSS-IGA020TC) and a 900 gr per mm grating blazed at 1.5 μm . Different samples were synthesized for each Yb/Er ratio. At least three spectra were collected for each sample. Then, we computed the average intensity of the spectra's integrated area within the green, red, or IR emission bands, for each ratio and we took the maximum deviation as the error. Results presented without error bars correspond to a single representative measurement.

To characterize the laser intensity at the sample, we measured the laser power with a thermal sensor power meter (Thorlabs, S310C) and the beam size using the slit-scan technique, being this size around 250 μm (full-width at half maximum).

Luminescence lifetimes were measured with the time-resolved photon counting method. The current laser controller generates 40 μs light excitation pulses with a repetition rate of 125 Hz. The Hamamatsu R928 photomultiplier tube that collects the luminescence signal is connected to a 50 Ohm input of a digital oscilloscope (Agilent, DSO9104A). The signal from the current laser controller is used to trigger the oscilloscope. A program (developed in Matlab) is used to analyze each signal obtained in real-time on the oscilloscope directly, and this code can simulate the discriminator and the multichannel counter. Upon analysis of more than 5000 trigger signals, we obtain a luminescence decay curve. The luminescence lifetime was obtained by fitting the decay curves to a single exponential function. For the fitting, we considered a time window from t_{ini} to t_{end} , where the final fitting time t_{end} was set long enough to allow the complete decay of luminescence (around $t_{\text{end}} = 2$ ms). For each experimental decay curve, we calculated around 25 fits by changing the initial fitting time t_{ini} within the range where the luminescence signal intensity varies from 70% to 30% of its maximum value. This fitting procedure gives us an average lifetime with its standard error.

3 Results and discussion

The emission properties of $\text{NaYF}_4\text{:Yb,Er}$ nanoparticles are highly dependent on their size, crystalline phase, and composition. It also depends on dopant distribution within the nanoparticles. To compare the effect of the dopant concentration properly, we have synthesized monodispersed nanoparticles based on the $\beta\text{-NaYF}_4\text{:Yb}_x\text{Er}_y$ with a total codoping concentration of 22% ($x+y = 0.22$), and varying the ratio between the Yb^{3+} and Er^{3+} ions (x/y) from 0 to 10 (see Table 1). Some representative ratios have been corroborated from EDS measurements and are included in Figure S1 (see ESI[†]). These nanoparticles have a mean size diameter of 30 ± 2 nm independently on the dopant concentration, as seen from TEM images (Figures 1A, 1E, 1I, and Figure S2 in ESI[†] where TEM images for all ratios has been included for completeness). HR-TEM images (Figures 1B, 1F, and 1J) obtained from the nanoparticles reveal their high crystallinity. In fact, crystal lattice fringe with a spacing value of $d = 0.524$ nm, which corresponds to the (100) crystal planes of $\beta\text{-NaYF}_4$ is obtained. Another effect that we have to consider is related to the ion distribution. Under some conditions, the different ion reactivity can induce an anisotropic distribution of the ions as previously published.³⁵ This result leads us to investigate the dopant distribution within the nanoparticles using elemental mapping analy-

ses. Figures 1C, 1G, and 1K and the elemental profile analysis shown in Figures 1D, 1H, and 1L prove that there is no appreciable changes in the distribution of ions within the particles for different Yb/Er ratios. Figure S3 (see ESI[†]) depicts the XRD diffraction pattern of the synthesized nanoparticles, showing that hexagonal β -phase reflections are obtained for all of them.

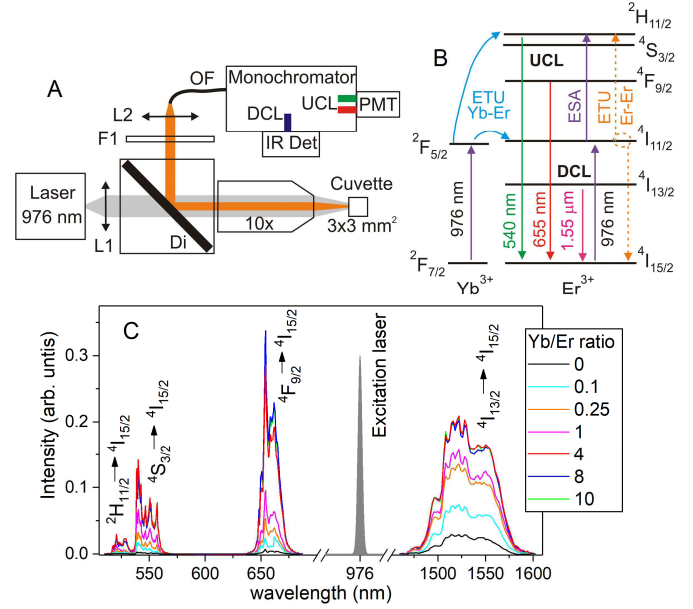


Fig. 2 (A) Scheme for the UCL and DCL detection setup: L1 collimating lens; Di long-pass dichroic filter; 10X microscope objective; F1 band-pass filter; L2 focusing lens; OF optical fiber; PMT photomultiplier tube; IR Det infrared detector. (B) Energy level diagram summarizing the biphotonic population pathways of the 520/540 nm green ($^2\text{H}_{11/2}$ and $^4\text{S}_{3/2} \rightarrow ^4\text{I}_{15/2}$) and 655 nm red ($^4\text{F}_{9/2} \rightarrow ^4\text{I}_{15/2}$) emission levels from Er^{3+} ions. The luminescence emission from these levels is represented by a solid green and red lines, respectively. A solid pink line represents the radiative downconversion luminescence. Purple lines represent the ground-state absorption for Yb^{3+} and Er^{3+} ions and excited-state absorption for Er^{3+} ions. Blue lines are energy transfer from Yb^{3+} ions to Er^{3+} ions. Dashed orange lines represent energy transfer between neighboring Er^{3+} ions. (C) Upconversion and downconversion luminescence spectra for different Yb/Er ratios. Excitation wavelength, 976 nm, and intensity of 5.3 kW/cm^2 with particle concentration of 1 mg/mL .

This information points out the absence of morphological and structural variations among the different nanoparticles, being possible to ascribe the photoluminescent variations mostly to the presence of a different concentration of dopants ions.

3.1 Luminescence variation with Yb/Er ratio

To analyze the role of the Yb/Er ratio on the luminescence properties of UCNPs, we measured, simultaneously, their UCL and DCL spectra under a NIR excitation CW laser at 976 nm. Results presented in Figure 2C show the spectra obtained from a 1 mg/mL hexane solution of UCNPs with different Yb/Er ratios excited with an intensity of 5.3 kW/cm^2 , above the typical saturation value of transition $^2\text{F}_{7/2} \rightarrow ^2\text{F}_{5/2}$ of the Yb^{3+} ions, which is $I_{\text{sat}}^Y = 3$ kW/cm^2 (see section 3.3). Different emission peaks are observed: two green emission peaks near 525 nm and 540 nm correspond-

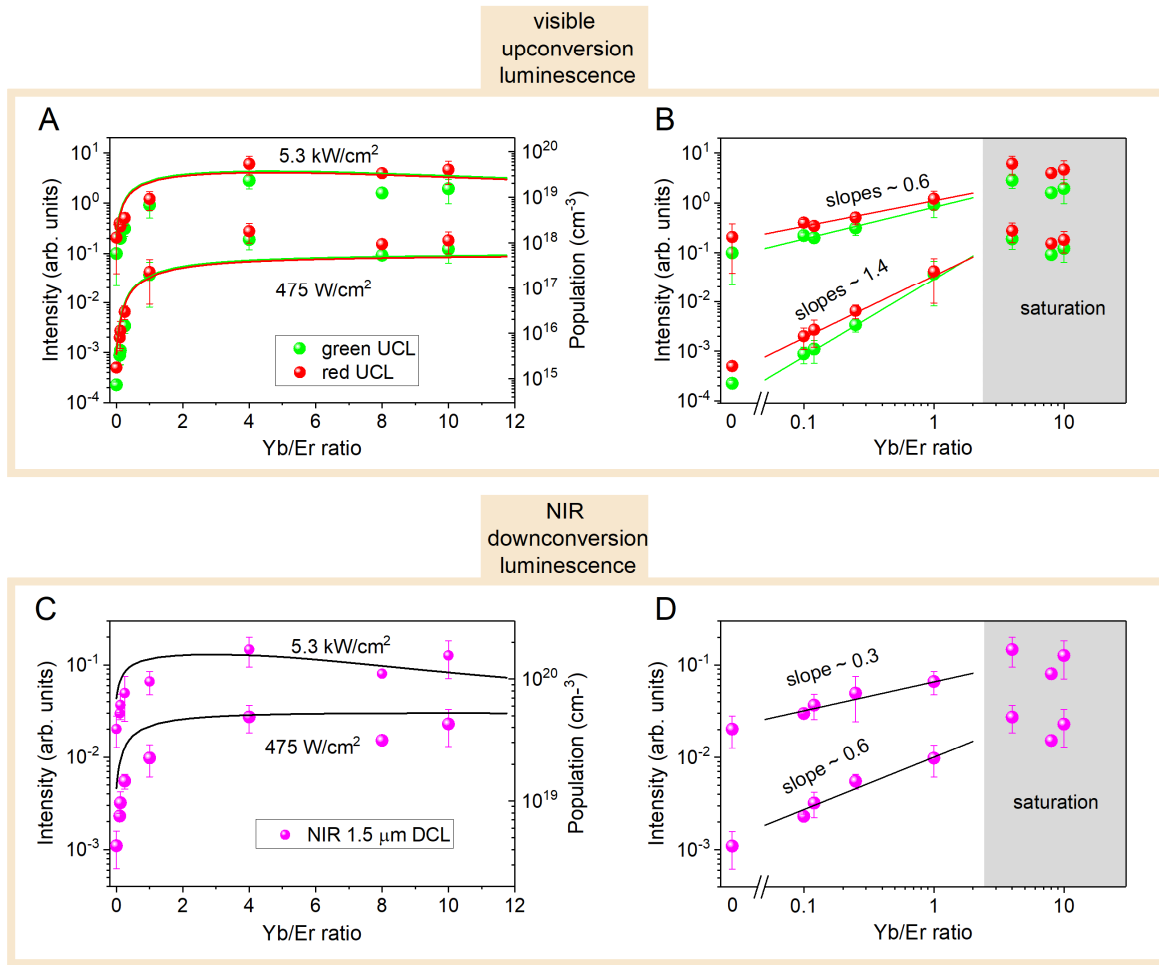


Fig. 3 Upconversion (A, B) and downconversion (C, D) integrated luminescence as a function of the Yb/Er ratio for two different excitation intensities, 475 W/cm² below saturation intensity, and 5.3 kW/cm² above saturation. Left panels (A, C) show the experimental data in the semi-log plot and the simulated intensity (solid line) from the rate equation model (Equation 1). Right panels (B, D) show a power-law behavior in a log-log plot and a saturation regime for Yb/Er ratios above 1. Ratio 0 has also been included in the log-log plot. Shadow areas show the ratios at which luminescence intensity is saturated.

ing to $^2H_{11/2} \rightarrow ^4I_{15/2}$ and $^4S_{3/2} \rightarrow ^4I_{15/2}$ transitions of the Er³⁺ ions, respectively; and a red emission peak around 655 nm corresponding to the $^4F_{9/2} \rightarrow ^4I_{15/2}$ transition of the Er³⁺ ions (see Figure 2B). Figure 2C also shows the downconversion luminescence of the NIR peak near 1.55 μm corresponding to the transition from the metastable level of Er³⁺ ions to their ground state, that is, $^4I_{13/2} \rightarrow ^4I_{15/2}$. In both cases, upconversion and downconversion luminescence, emission strongly increases with the Yb/Er ratio. However, above a ratio of 4, no further increase is observed. Note that the range of Er³⁺ and Yb³⁺ concentrations investigated here varies from an Er³⁺ dopant concentration of 22% (ratio 0) where only Er³⁺ ions are present to the well-known standard ratio of 20% of Yb³⁺ and 2% of Er³⁺ (ratio 10). Thus, within this broad dopant range different photon upconversion mechanisms are expected to take place. Figure 2B shows different population pathways of the UCL emission bands. In the standard case of 20% of Yb³⁺ and 2% of Er³⁺ (ratio 10), the energy transfer from Yb³⁺ ions to Er³⁺ ions should dominate. However, when only Er³⁺ ions are present, excited-state absorption from $^4I_{11/2}$ level or energy

transfer between neighboring Er³⁺ ions should be responsible for the UCL emission. On the other hand, the DCL can be achieved by ground-state absorption (GSA) of laser photons by both Er³⁺ and Yb³⁺ ions.

To develop more quantitative analysis, we show in Figures 3A and 3B the integrated spectra of the green and red bands as a function of the Yb/Er ratio for two different excitation intensities, 475 W/cm² below the Yb³⁺ saturation intensity, and 5.3 kW/cm² above saturation. Both emission bands show similar behavior, a vast increase in luminescence intensity up to a saturation value reached for Yb/Er ratios above 1 (see semi-log plot in Figure 3A). A broader variation range (three orders of magnitude difference in luminescence) is observed at low excitation intensities (475 W/cm²) than at high excitation intensities (5.3 kW/cm²), where a two-fold variation range is achieved. This phenomenon can be better visualized in the log-log plot in Figure 3B. We found that UCL intensity increases following a power-law behavior with Yb/Er ratio for ratios below 1. The power-law exponent depends on the excitation intensity. A larger exponent is achieved for the

linear absorption regime (below the saturation intensity), which produces the greatest luminescence intensity variation mentioned above.

In Figures 3C and D, the integrated downconversion spectra are also shown. We observed similar behavior than for the upconversion luminescence (see semi-log plot in Figure 3C). Again, larger luminescence intensity variation occurs at low laser irradiances, as shown in the log-log plot in Figure 3D. Note that the power-law exponents found for the DCL are smaller than the ones corresponding to the UCL. Therefore, the upconversion phenomenon is more strongly affected by the Yb/Er ratio variation than the downconversion luminescence.

In summary, contrary to what is normally assumed, there is not a critical Yb/Er ratio that maximize the luminescence intensity (usually established as ratio 10), but a wider range of ratios from around 2 to 10 which lead to roughly the same luminescence intensity value. Furthermore, a very slightly decrease in intensity occurs above ratio 4 which corresponds to a fraction of doped ions of 17.6% of Yb^{3+} and 4.4% of Er^{3+} .

As pointed out, the variation of luminescence with excitation power is greater at low Yb/Er ratios, which could indicate a saturation of luminescence at high Yb/Er ratios. To confirm this, we analyzed the dependence of the green and red luminescence

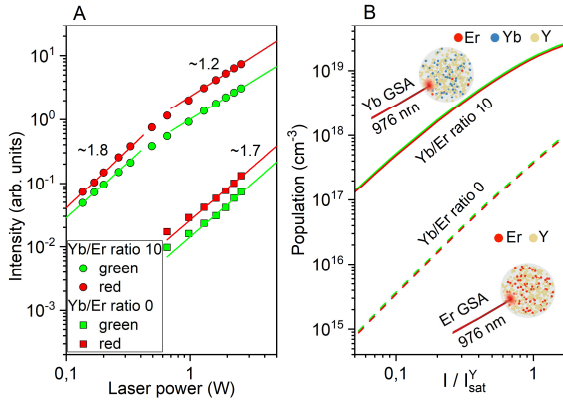


Fig. 4 (A) Green and red upconversion integrated luminescence as a function of the laser power for two extreme Yb/Er ratios: 0 (squares) and 10 (circles). The solid lines are linear fits to the data. (B) Simulated curves: steady-state population of the green and red emission levels as a function of the normalized excitation intensity for Yb/Er ratio 10 (solid lines) and ratio 0 (dashed lines). UCNP pictures show the proportion of ions for these two Yb/Er ratios indicating, in each case, the ion responsible for the excitation absorption: ~ 1.7 GSA for ratio 10, and Er^{3+} GSA for ratio 0.

with the excitation intensity for the two extreme Yb/Er ratios, 10 and 0 (see Figure. 4). For ratio 10 (see circles), a biphotonic process is obtained (power-law exponent close to 2) at excitation intensities below the saturation value of the Yb^{3+} transition. This quadratic behavior points out the nature of the underlying up-conversion mechanism: two laser photons are needed to obtain a visible emitted photon. However, at excitation intensities above the saturation one, the quadratic behavior saturates due to the absorption saturation of the Yb^{3+} transition leading to an exponent closer to one. For Yb/Er ratio 0 (see squares), the quadratic

behavior (biphotonic process) remains for all the excitation powers. In this case, the first step of the UCL emission is through the ground state absorption of the $^4\text{I}_{15/2} \rightarrow ^4\text{I}_{11/2}$ transition from Er^{3+} . This transition has a larger saturation intensity, which is not reached by the laser power used in the experiments, and therefore it is still operating in the linear absorption regime.

3.2 Time-resolved luminescence analysis

Let us now analyze the time-resolved UCL for the UCNP's with different Yb/Er ratios. Figure 5 shows the luminescence decay curves at both UCL bands: green band at 539 nm and red band at 654 nm. Luminescence signals coming from UCNP's at different ratios roughly match each other, which in principle indicates a negligible influence of the Yb/Er ratio. We obtained a lifetime of around 127 μs for the green UCL and around 227 μs for the red UCL. Therefore, the Yb/Er ratio does not significantly affect the UCL emission's decay dynamics. The results will support the idea that the UCL intensity depends on how efficiently is populated the corresponding green-emitting or red-emitting levels in terms of the total number of sensitizers (Yb^{3+} ions) and emitters (Er^{3+}). The decay curves in Figure 5 show an initial increase that is a signature of the upconversion process by means of energy transfer from Yb^{3+} to Er^{3+} ions. Interestingly, this initial luminescence increase also appears when decreasing Yb/Er ratio, even at ratio 0, where only Er^{3+} ions are present. This result indicates that an energy transfer process occurs between neighboring Er^{3+} ions, which will compete with the excited state absorption process.

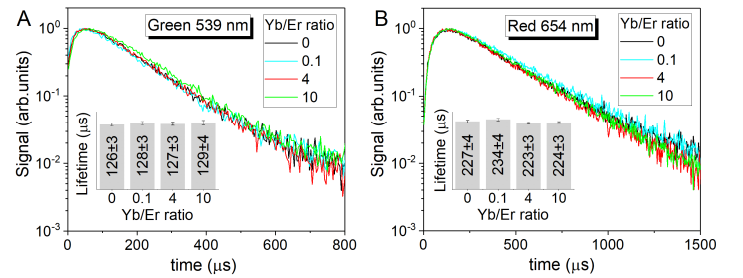


Fig. 5 (A) Green and (B) red upconversion luminescence decay signals for UCNP's with different Yb/Er ratio. (Inset) Lifetime values obtained by exponential fitting of the decay curves.

3.3 Rate equation analysis

Let us theoretically interpret the steady-state luminescence experiments by performing a rate equation analysis. We used the following rate equation model, which describes the main physical mechanisms of our system (see details in Figure 6):

$$\begin{aligned}
\frac{dN_1}{dt} &= -W_1 N_1 + W_{21} N_2 - K_3 N_1 N_1^Y - \frac{\sigma_{13}}{\sigma_{02}} \frac{W_1 I}{I_{sat}} (N_1 - N_3) - 2C_1 N_1^2, \\
\frac{dN_2}{dt} &= -W_2 N_2 + W_{32} N_3 + K_2 N_0 N_1^Y - K_{B2} N_2 N_0^Y - K_4 N_2 N_1^Y \\
&\quad + \frac{W_1 I}{I_{sat}} (N_0 - N_2) - \frac{\sigma_{24}}{\sigma_{02}} \frac{W_1 I}{I_{sat}} N_2 + C_1 N_1^2 - 2C_2 N_2^2, \\
\frac{dN_3}{dt} &= -W_3 N_3 + W_{43} N_4 + K_3 N_1 N_1^Y + \frac{\sigma_{13}}{\sigma_{02}} \frac{W_1 I}{I_{sat}} (N_1 - N_3), \\
\frac{dN_4}{dt} &= -W_4 N_4 + K_4 N_2 N_1^Y + \frac{\sigma_{24}}{\sigma_{02}} \frac{W_1 I}{I_{sat}} N_2 + C_2 N_2^2, \\
\frac{dN_1^Y}{dt} &= -W_1^Y N_1^Y + \frac{W_1^Y I}{2I_{sat}^Y} (N_0^Y - N_1^Y) - K_2 N_0 N_1^Y + K_{B2} N_2 N_0^Y \\
&\quad - K_3 N_1 N_1^Y - K_4 N_2 N_1^Y.
\end{aligned}
\tag{1}$$

Here N_j is the density of Er^{3+} ions in the energy level j , where the subscripts $j = 0, 1, 2, 3$, and 4 represent the $^4I_{15/2}$, $^4I_{13/2}$, $^4I_{11/2}$, $^4F_{9/2}$, and $^4S_{3/2}$ energy levels of Er^{3+} ions, respectively (see Figure 6). The population of fast-decaying levels as $^4F_{7/2}$ and $^4I_{9/2}$ were neglected and the populations of energy levels $^2H_{11/2}$ and $^4S_{3/2}$ are in thermal equilibrium. N_0^Y and N_1^Y are the Yb^{3+} ions density in the $^2F_{7/2}$ and $^2F_{5/2}$ energy levels. W_{jl} is the decay rate from level j to level l whereas W_j (W_j^Y for Yb^{3+} ions) is the total decay rate of the energy level j . The decay rates from an excited-level to the ground state were considered as radiative decay rates (in the millisecond range) and the corresponding to the next lower level as a faster nonradiative decay (microsecond range) through multi-phonon relaxation. On the other hand, K_2 , K_3 and K_4 are the coefficients of the resonant energy transfer from the Yb^{3+} ion (sensitizer) to levels 2, 3, and 4 of the Er^{3+} ion (activator), respectively. K_{B2} is the coefficient of back energy transfer from the Er^{3+} ion in level 2 to the Yb^{3+} ion. C_1 and C_2 are the coefficients of energy transfer between neighbors Er^{3+} ions. C_1 represents a quenching mechanism for erbium-doped amplifiers ($^4I_{13/2}$, $^4I_{13/2}$) \rightarrow ($^4I_{15/2}$, $^4I_{9/2}$) and C_2 represents an upconversion energy transfer to the green-emitting level ($^4I_{11/2}$, $^4I_{11/2}$) \rightarrow ($^4I_{15/2}$, $^4F_{7/2}$). σ_{jl} is the absorption (\simeq emission) cross-section at the laser frequency for transition from level j to level l of Er^{3+} ions. The absorption cross-section of Yb^{3+} transition is σ^Y . The laser intensity is denoted as I (in units of W/cm^2) and is normalized to the saturation intensity $I_{sat}^Y = \hbar\omega W_1^Y / (2\sigma^Y)$ for Yb^{3+} transition and to $I_{sat} = \hbar\omega W_1 / \sigma_{02}$ for Er^{3+} transitions, where $\hbar\omega$ is the transition energy (resonant with the excitation laser wavelength at 976 nm).

In our simulations, we considered decay, energy transfer coefficient, and absorption cross-section values of the same order of magnitude as those found in literature^{26,36–38} (see Sec. S4 in ESI[†]). By numerically solving Equation 1 we obtained the steady-state populations which allowed us to compute the luminescence intensity. We plotted the simulated UCL and DCL intensities (see lines in Figures 3A and 3C, respectively) as a function of the Yb/Er ratio for a laser intensity below ($I/I_{sat}^Y = 0.1$)

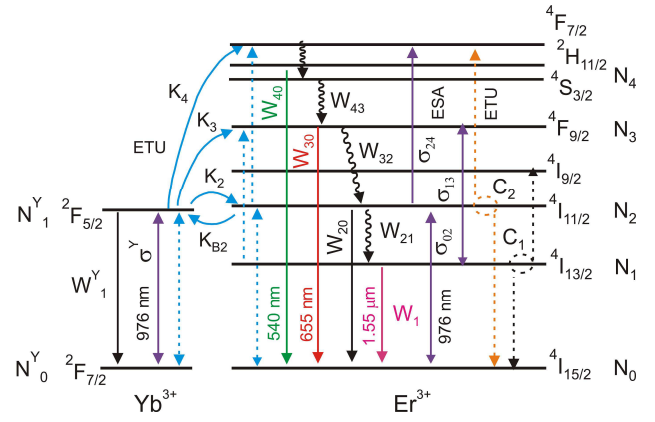


Fig. 6 Energy level diagram for Yb^{3+} and Er^{3+} ions describing the physical processes used in our rate equation model. Blue lines represent the Yb-Er ETU mechanism (K_2 , K_{B2} , K_3 , K_4), whereas orange and black dashed lines represent different Er-Er ETU mechanisms (C_2 and C_1). Purple lines represent ground state absorption of Yb^{3+} (σ^Y) and Er^{3+} (σ_{02}) ions, and excited-state absorption of Er^{3+} ions (σ_{13} and σ_{24}). Solid lines represent radiative decay rates from different levels (W_1^Y for Yb^{3+} and W_1 , W_{20} , W_{30} , W_{40} for Er^{3+}), whereas faster nonradiative decay rates are represented by wavy lines (W_{43} , W_{32} , W_{21}).

and above ($I/I_{sat}^Y = 2$) the saturation intensity of the Yb transition. These simulated curves showed very good agreement with the experimental results. Furthermore, we theoretically analyzed the biphotonic behavior of the upconversion mechanism for the Yb/Er ratios used in Figure 4A. Then, we computed the population of the green ($^4S_{3/2}$) N_4 and red ($^4F_{9/2}$) N_3 emission levels as a function of the excitation intensity. The results, shown in Figure 4B, showed the same behavior as the one reported in the experiments. For Yb/Er ratio 0, the laser always operates in the linear absorption regime since the excitation intensity is below the saturation value of the ground state absorption of Er^{3+} transition $^4I_{15/2} \rightarrow ^4I_{11/2}$. Therefore, the quadratic behavior remains. However, for Yb/Er ratio 10 the laser absorption is due to the ground state absorption of Yb^{3+} transition $^2F_{7/2} \rightarrow ^2F_{5/2}$. This transition exhibits lower saturation value so that it can be reached with the excitation laser intensity used in the experiments, and therefore a saturation of the quadratic behavior occurs.

Finally, we used our theoretical model to analyze the contribution of the different mechanisms leading to upconversion emission as a function of the Yb/Er ratio. Equation 1 was solved by allowing independently only one of the three possible pathways that populate the green and red emission levels: 1) ETU from Yb^{3+} ions to Er^{3+} ions (ETU Yb-Er) which is controlled by parameters K_2 and K_4 ; 2) ESA from $^4I_{11/2}$ level of Er^{3+} ions which is controlled by the parameter σ_{24} ; and 3) ETU between neighboring Er^{3+} ions (ETU Er-Er) which is controlled by the parameter C_2 . Figure 7A shows the population of the green emission level N_4 as a function of the Yb/Er ratio when only one of the mechanisms is present at a time. For example, red curve corresponds to ETU Yb-Er and was obtained by setting $\sigma_{24} = 0$ and $C_2 = 0$ in the simulations. We also plotted in the same figure the result obtained when all the processes were present. We observed how the dominant mechanism of upconversion changes as the Yb/Er

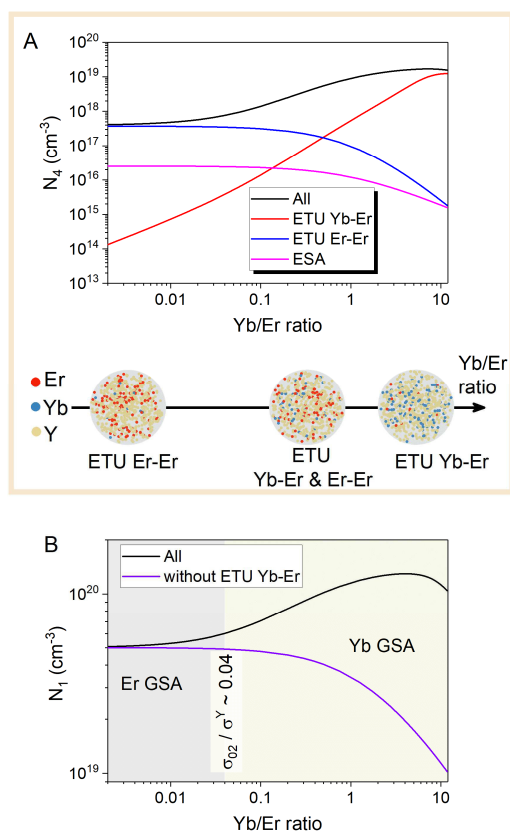


Fig. 7 (A) (up) Steady-state population of the green emission level ($^4S_{3/2}$) N_4 of Er^{3+} ions as a function of the Yb/Er ratio for a laser intensity $I/I_{\text{sat}}^Y = 1$. Different curves were computed using different pathways that populate the green and red emission levels. (down) Picture of UCNPs with different Er^{3+} and Yb^{3+} ion concentration indicating below them the dominant upconversion mechanism in each case. (B) Steady-state population of the NIR emission level ($^4I_{13/2}$) N_1 of Er^{3+} ions as a function of the Yb/Er ratio for a laser intensity $I/I_{\text{sat}}^Y = 1$. Curves were computed with and without accounting for Yb/Er ETU mechanism.

ratio varies. For very low Yb/Er ratios, ETU Yb-Er was negligible as expected since there were very few Yb^{3+} ions to transfer their energy to the Er^{3+} ions. In this regime, we found that the primary mechanism of upconversion was the energy transfer between Er^{3+} ions, instead of the ESA process. On the other hand, at large values of the Yb/Er ratio, ETU Yb-Er was the dominant mechanism, as expected. When the Yb/Er ratio was close to 1, i.e. similar dopant concentrations, the two mechanisms (ETU Er-Er and ETU Yb-Er) compete.

We have also analyzed the competition between the two mechanism leading to DCL, that is, the GSA of Er^{3+} ions and the GSA of Yb^{3+} ions. To do that we computed the steady-state population of the $^4I_{13/2}$ level of Er^{3+} ions with and without considering ETU from Yb^{3+} ions to Er^{3+} ions. The result was shown in Figure 7B. The NIR emission at $1.55 \mu\text{m}$ was mainly achieved thanks to the energy transfer from Yb^{3+} ions to Er^{3+} ions even for very low values of the Yb/Er ratio (≈ 0.04). As the ground state absorption cross section of Yb^{3+} ions is more than one order of magnitude larger than the corresponding to Er^{3+} ions, even at very low Yb/Er ratio, the global absorption can be ascribed to Yb^{3+} ions. How-

ever, for Yb/Er ratios below 0.04, the small number of Yb^{3+} ions in the UCNPs are not able to populate the Er^{3+} ions. Therefore, the only mechanism leading to DCL is the GSA of Er^{3+} ions. As a summary, the combination of both ground state absorption cross sections and concentrations of activators and sensitizers decide which ion absorbs NIR radiation more efficiently.

4 Conclusions

In this work, we studied the performance of UCL and DCL emission of 30 nm monodisperse $\beta\text{-NaYF}_4: \text{Yb}^{3+}, \text{Er}^{3+}$ nanoparticles with a fixed total amount of dopants in the matrix. In particular, we focused on the role of dopant concentration, replacing 22% of the Y^{3+} ions with a variable ratio of Yb^{3+} ions to Er^{3+} ions between 0 and 10. In both cases (UCL and DCL), the luminescence emission increased considerably as Yb/Er ratio increased. However, for ratios greater than four, no additional increase was noted. Larger variation in UCL and DCL was observed when decreasing excitation intensity. Time-resolved luminescence analyzed in UCL did not show any appreciable change with dopant ratio, indicating a negligible effect of the dopant ratio on the decay dynamics of the UCL emission.

Finally, a theoretical model was used to analyze the contribution of the different mechanisms involved in UCL and DCL when dopant ratio was varied. According to the results, we confirmed that UCL's dominant mechanism varied with the Yb/Er ratio. For very low Yb/Er ratios, the ETU Er-Yb was negligible, and the ETU Er-Er process took precedence even over the ESA. In ratio 1, where the dopants' concentration was the same, there was a competition between ETU Yb-Er and ETU Er-Er. In ratio 10, as expected, the predominant mechanism was the ETU Yb-Er. The DCL emission in the NIR at 1550 nm was achieved mainly thanks to the Yb^{3+} ions' transfer of energy to the Er^{3+} ions. It can be concluded that there was a competition between the GSAs of both types of ions and their concentrations. However, as the Yb^{3+} ions GSA was one order of magnitude greater than that of the Er^{3+} ions, the overall absorption was attributed to the Yb^{3+} ions, even for the lowest, except 0, analyzed Yb/Er ratio of 0.1.

Conflicts of interest

There are no conflicts to declare.

Acknowledgements

This work was supported by Ministerio de Economía y Competitividad-MINECO (MAT2016-75955, MAT2017-83111R, PID2019-106820RB-C21), and Comunidad de Madrid (B2017/BMD-3867 RENIM-CM). We also acknowledge Colfuturo and the Colombian government for V.T predoctoral scholarship, as well as to UCM and Santander bank for D. M-G postdoctoral contract (CT 17/17-CT18/17). D-J. R. R. thanks to European Commission for YEI program contract (PEJD-2018-PRE/IND-9118). TEM images were obtained at the National Center for Electron Microscopy (UCM, Madrid).

Notes and references

- 1 F. Auzel, *Chemical Reviews*, 2004, **104**, 139–174.

- 2 M. Haase and H. Schäfer, *Angewandte Chemie International Edition*, 2011, **50**, 5808–5829.
- 3 F. Wang, R. Deng, J. Wang, Q. Wang, Y. Han, H. Zhu, X. Chen and X. Liu, *Nature Materials*, 2011, **10**, 968–973.
- 4 D. K. Chatterjee, A. J. Rufaihah and Y. Zhang, *Biomaterials*, 2008, **29**, 937 – 943.
- 5 G. Chen, H. Qiu, P. N. Prasad and X. Chen, *Chemical Reviews*, 2014, **114**, 5161–5214.
- 6 D. Mendez-Gonzalez, M. Laurenti, A. Latorre, A. Somoza, A. Vazquez, A. I. Negredo, E. López-Cabarcos, O. G. Calderón, S. Melle and J. Rubio-Retama, *ACS Applied Materials & Interfaces*, 2017, **9**, 12272–12281.
- 7 M. You, J. Zhong, Y. Hong, Z. Duan, M. Lin and F. Xu, *Nanoscale*, 2015, **7**, 4423–4431.
- 8 M. Schoenauer Sebag, Z. Hu, K. de Oliveira Lima, H. Xiang, P. Gredin, M. Mortier, L. Billot, L. Aigouy and Z. Chen, *ACS Applied Energy Materials*, 2018, **1**, 3537–3543.
- 9 P. Alonso-Cristobal, O. Oton-Fernandez, D. Mendez-Gonzalez, J. F. Díaz, E. Lopez-Cabarcos, I. Barasoain and J. Rubio-Retama, *ACS Applied Materials & Interfaces*, 2015, **7**, 14992–14999.
- 10 D. Jaque and F. Vetrone, *Nanoscale*, 2012, **4**, 4301–4326.
- 11 A. Gnach and A. Bednarkiewicz, *Nano Today*, 2012, **7**, 532–563.
- 12 G. Chen, C. Yang and P. N. Prasad, *Accounts of Chemical Research*, 2013, **46**, 1474–1486.
- 13 F. Wang and X. Liu, *Chem. Soc. Rev.*, 2009, **38**, 976–989.
- 14 J. Suyver, J. Grimm, M. van Veen, D. Biner, K. Krämer and H. Güdel, *Journal of Luminescence*, 2006, **117**, 1 – 12.
- 15 S. Schietinger, L. d. S. Menezes, B. Lauritzen and O. Benson, *Nano Letters*, 2009, **9**, 2477–2481.
- 16 D. T. Klier and M. U. Kumke, *J. Mater. Chem. C*, 2015, **3**, 11228–11238.
- 17 S. Fischer, B. Fröhlich, K. W. Krämer and J. C. Goldschmidt, *The Journal of Physical Chemistry C*, 2014, **118**, 30106–30114.
- 18 S. Wilhelm, *ACS Nano*, 2017, **11**, 10644–10653.
- 19 C. T. Xu, Q. Zhan, H. Liu, G. Somesfalean, J. Qian, S. He and S. Andersson-Engels, *Laser & Photonics Reviews*, 2013, **7**, 663–697.
- 20 M. Wang, Y. Tian, F. Zhao, R. Li, W. You, Z. Fang, X. Chen, W. Huang and Q. Ju, *J. Mater. Chem. C*, 2017, **5**, 1537–1543.
- 21 K. W. Krämer, D. Biner, G. Frei, H. U. Güdel, M. P. Hehlen and S. R. Lüthi, *Chemistry of Materials*, 2004, **16**, 1244–1251.
- 22 C. Rennero-Lecuna, R. Martín-Rodríguez, R. Valiente, J. González, F. Rodríguez, K. W. Krämer and H. U. Güdel, *Chemistry of Materials*, 2011, **23**, 3442–3448.
- 23 Y. Wang, R. Deng, X. Xie, L. Huang and X. Liu, *Nanoscale*, 2016, **8**, 6666–6673.
- 24 S. Wen, J. Zhou, K. Zheng, A. Bednarkiewicz, X. Liu and D. Jin, *Nature Communications*, 2018, **9**, 2415.
- 25 B. Cao, Y. He, L. Zhang and B. Dong, *Journal of Luminescence*, 2013, **135**, 128 – 132.
- 26 M. Kaiser, C. Würth, M. Kraft, T. Soukka and U. Resch-Genger, *Nano Research*, 2019, **12**, 1871–1879.
- 27 T. D. Cao, T. G. Le, T. N. Nguyen, T. N. Dau, V. T. Nguyen and T. V. Tran, *Journal of Molecular Structure*, 2020, **1210**, 128014.
- 28 B. Shen, S. Cheng, Y. Gu, D. Ni, Y. Gao, Q. Su, W. Feng and F. Li, *Nanoscale*, 2017, **9**, 1964–1971.
- 29 C. Ma, X. Xu, F. Wang, Z. Zhou, D. Liu, J. Zhao, M. Guan, C. I. Lang and D. Jin, *Nano Letters*, 2017, **17**, 2858–2864.
- 30 M. Kamimura, N. Kanayama, K. Tokuzen, K. Soga and Y. Nagasaki, *Nanoscale*, 2011, **3**, 3705–3713.
- 31 J. Hu, Y. Zhang, H. Xia, H. Ye, B. Chen and Y. Zhu, *Inorganic Chemistry*, 2018, **57**, 7792–7796.
- 32 X. Chen, Y. Zhu, D. Zhou, W. Xu, J. Zhu, G. Pan, Z. Yin, H. Wang, S. Cui and H. Song, *J. Mater. Chem. C*, 2017, **5**, 2451–2458.
- 33 M. Lin, Y. Zhao, S. Wang, M. Liu, Z. Duan, Y. Chen, F. Li, F. Xu and T. Lu, *Biotechnology Advances*, 2012, **30**, 1551 – 1561.
- 34 S. Melle, O. G. Calderón, M. Laurenti, D. Mendez-Gonzalez, A. Egatz-Gómez, E. López-Cabarcos, E. Cabrera-Granado, E. Díaz and J. Rubio-Retama, *The Journal of Physical Chemistry C*, 2018, **122**, 18751–18758.
- 35 R. Shi, X. Ling, X. Li, L. Zhang, M. Lu, X. Xie, L. Huang and W. Huang, *Nanoscale*, 2017, **9**, 13739–13746.
- 36 R. B. Anderson, S. J. Smith, P. S. May and M. T. Berry, *The Journal of Physical Chemistry Letters*, 2014, **5**, 36–42.
- 37 N. U. Wetter, A. M. Deana, I. M. Ranieri, L. Gomes and S. L. Baldochi, *IEEE Journal of Quantum Electronics*, 2010, **46**, 99–104.
- 38 S. Fischer, H. Steinkemper, P. Löper, M. Hermle and J. C. Goldschmidt, *Journal of Applied Physics*, 2012, **111**, 013109.